DNS OF A HYPERSONIC FLOW ON A RAMP GEOMETRY WITH ISOLATED ROUGHNESS

Giuseppe Chiapparino and Christian Stemmer

Chair of Aerodynamics and Fluid Mechanics
Technische Universität München
Boltzmannstr. 15, 85748 Garching b. München, Germany

ABSTRACT

A Mach 6 flow over a $10°$ compression corner is investigated by Direct Numerical Simulations. A roughness patch made of sinusoidal elements is placed at two different positions upstream of the smooth-separation location in order to investigate its effects on the separation bubble. Flow separation is delayed with respect to the smooth case and the streamwise vortices induced by the patch generate a mushroom-like structure once the flow reattaches on the ramp. This structure leaves high-temperature streaks on the wall of the ramp, at the same time causing hot flow to be pushed into the freestream. When excited by freestream acoustic disturbances at 100kHz, the structure in the wake of the roughness starts to break down on the ramp, leading to a further increase in wall temperature.

Index Terms— Hypersonic boundary-layer flow, roughness patch, separation region, compression corner

1. INTRODUCTION

Surface roughness plays a fundamental role in laminar-turbulent boundary-layer transition, especially in the case of hypersonic flows characterizing high-speed aircraft such as scramjets and re-entry capsules. These vehicles need to withstand prohibitive conditions as they fly through the atmosphere because of the strong mechanical and thermal stresses imposed by the shock-waves forming close to their surface. Furthermore, these conditions often favour chemical reactions within the flow, like molecular dissociation and recombination, with further effects on the aircraft [1]. In this scenario, the boundary-layer flow regime is a key factor in determining the surface heat-flux on the wall of the vehicle. It is known that a turbulent boundary layer induces a higher heat exchange with respect to a laminar one. However, in case of transitional flows, even higher rates can be achieved [2]. While boundary-layer transition may happen naturally over smooth surfaces, the presence of roughness elements, as a result of manufacturing imperfections, small gaps/steps between tiles or ablation, is known to have considerable effects on the boundary-layer stability. If the roughness is high enough, it can directly trigger the transition of a laminar flow to the turbulent state. Experimentally [3], for example, this

was found to happen for Mach 4.8 and 6 flat-plate boundary layers with roughness elements (spheres, in that case) twice as high as the local boundary-layer thickness. The shape of the elements appears to be a factor that can affect the ability to trip the flow, as emerged by experimental comparisons between spherical and triangular elements [4], the latter becoming effective at lower Reynolds numbers. Usually, roughness, whether isolated or distributed, that causes immediate flow transition is said to be "effective", while it is called "critical" if its size starts to affect transition position with respect to the smooth case [5]. At hypersonic speeds, transition is affected once the roughness reaches very large heights compared to the boundary-layer thickness. These effects, in most of the cases, consist in moving the transition point forward (i.e. towards the roughness location) and are more evident as the roughness height increases (until it becomes effective). The reason is that roughness can make the flow in its wake more unstable, allowing freestream disturbances to grow in amplitude, eventually leading to transition earlier than in the natural case. This was experimentally demonstrated at low speeds [6], where the presence of surface waviness with a well-defined wavenumber spectrum led to an increase of the receptivity coefficients of a Blasius boundary layer excited by TS waves. As for hypersonic boundary layers, the effect of isolated roughness elements was numerically investigated for a Mach 6 flat plate [7]. Several parameters like height, planform, front and streamwise shapes were analysed in order to assess their effect on transition. The latter two parameters were the most influential for flow breakdown. Moreover, a direct relation was found between the maximum amplitude of the streaks forming behind the elements and the exponential growth rate of instabilities in the roughness wake. The experimental investigation of multiple asymmetric isolated elements on a supersonic flat plate [8] showed that the relative position of such elements can have an impact on transition location and stability properties of the wake flow. Together with flat-plate geometries, several experimental and numerical investigations on the role of roughness in transition mechanisms have been performed for other geometries like cones and blunt bodies [9, 10, 11]. As mentioned, roughness often promotes transition. However, some investigations [3, 12, 13] suggested also that, under certain conditions,

roughness elements smaller than the boundary-layer thickness could slightly delay transition with respect to the natural (i.e. smooth) scenario.

Hence, the role of roughness in laminar-turbulent transition at high speeds is far from being completely understood. This work aims at investigating the effect of isolated roughness elements in hypersonic ramp flows. This type of geometry is generally used to model control flaps or engine intakes of high-speed vehicles. Under hypersonic conditions, the strong ramp-induced oblique-shock interacts with the incoming boundary layer. The consequent Shock-Wave/Boundary-Layer Interaction (SWBLI) [14] might result in the separation of the boundary layer well upstream of the corner, with an associated separation shock. The detached shear layer then convects downstream, eventually reattaching on the ramp, generating a reattachment shock. Hence, the separation bubble forms in the region limited by the two shocks, the shear layer and the wall. For two-dimensional ramp geometries, secondary separations can be present within the separation bubble, with the consequent formation of multiple vortices in the recirculation region [15, 16, 17]. This phenomenon is more evident for long separation bubbles (i.e. comparable to the length of the flat part in front of the ramp [18]) which form at higher ramp angles. In these cases, the Stanton number and skin-friction distributions at the wall show secondary peaks in correspondence to the smaller vortices within the bubble. However, if the ramp angle exceeds certain values the separation bubble might become unstable and, after introducing freestream disturbances upstream of the boundary-layer separation, the flow shows a three-dimensional behaviour. Corrugations appear on the reattachment line, with streamlines generating nodes and saddle points in its proximity, and streamwise streaks form in the fully reattached flow [19, 20]. Amplification due to mechanisms like Görtler instability can eventually lead to transition further downstream along the ramp. A similar flow behaviour can be observed in the case of an impinging shock over a flat plate. Provided that the boundary layer experiences a comparable pressure rise due to the incoming shock, this case is equivalent to the ramp one [14]. Hence, also separation bubbles that form for such geometries may become unstable for high impinging angles [21, 22] and the critical modes can be computed, for example, by means of global stability analysis.

The influence of roughness elements on laminar ramp configurations has been investigated in a number of recent works, in both two-dimensional [23, 17] and three-dimensional [24] setups. In latter case, an array of roughness elements is placed ahead of successive small compression corners of an engine intake. The trips induce the formation of steady mushroom-shaped structures, which become more evident once they pass onto the following ramp. As a consequence, streamwise streaks are produced downstream of the roughness, with effects on the heat flux at the wall. In the wake of the trips, both odd (sinuous) and even (varicose)

modes were identified, with the former being the most unstable ones. It is concluded that, for trip heights between the critical and effective values, the roughness-induced streak instability might play a role in transition. It is worth noting that, in those investigations [24], the ramp angles were too small to generate clear recirculation regions at the corners.

The present work focuses on the effect of isolated roughness patches placed upstream of compression corners capable of generating large separation bubbles.

2. METHODOLOGY

2.1. Setup and Geometry

This paper focuses on a $M_\infty = 6$ hypersonic flow over a $\theta = 10°$ compression corner. Freestream conditions, marked with the subscript ∞, are taken at a reference altitude $h_\infty = 25km$ for standard air and are listed in table 1.

Table 1. Freestream conditions at reference altitude.

Parameter	Value	Parameter	Value
T_∞	220 [K]	μ_∞	$1.44 \cdot 10^{-5}$ [Pa·s]
p_∞	2500 [Pa]	ρ_∞	0.0396 [Kg/m^3]
M_∞	6	u_∞	1783.89 [m/s]

The freestream and geometrical conditions considered here represent plausible operational conditions for control surfaces of high-speed aircraft studied over the last years (as in the HEXAFLY-INT project [25]). The dimensions of the computational domain are $L_x = 0.490m$, $L_y = 0.065m$ and $L_z = 0.021m$ in the streamwise, wall-normal and spanwise directions, respectively. The reference system originates at the inflow, on the lower corner of the domain, as shown by the blue square in figure 1. The compression corner is situated at $L_c = 0.300m$ downstream of the inflow. The dimensions of the computational domain are the same for both the smooth and the rough cases. However, in the latter ones, a three-dimensional roughness patch is modelled by directly modifying the grid-surface height at the wall. The roughness is "isolated" in the sense that the patch covers a very limited portion of the domain. Nonetheless, it is made of a number of streamwise and spanwise sinusoidal elements. Its surface height is computed with the following formula:

$$h_k(x, z) = k \cdot f_1 \cdot \sin\left[\frac{\pi(x - x_i)}{I_x/E_x}\right] \cdot \sin\left[\frac{\pi(z - z_i)}{I_z/E_z}\right]. \quad (1)$$

I_x and I_z indicate the streamwise length and the spanwise width of the patch, respectively. E_x and E_z represent the number of half-sinusoidal elements in the x- and z-directions. The piecewise function $f_1 = f_1(x, z)$ limits the patch to the rectangular area defined by $[x_i, x_i + I_x]$ and $[z_i, z_i + I_z]$, with $x_i = x_k - I_x/2$ and $z_i = z_k - I_z/2$ being the lower limits of the patch. Two different patch positions are considered.

The first, labelled $RP1$ is closer to the inflow, while the second, $RP2$, is placed further downstream, but still ahead of the smooth boundary-layer separation point. The centres of the patches are placed at $(x_k, z_k)_{RP1} = (0.0461, 0.0105)m$ and $(x_k, z_k)_{RP2} = (0.0936, 0.0105)m$, respectively. A third patch ($RP3$), placed at $(x_k, z_k)_{RP3} = (0.2499, 0.0105)m$ did not change the scenario from the smooth case significantly, and was hence omitted here.
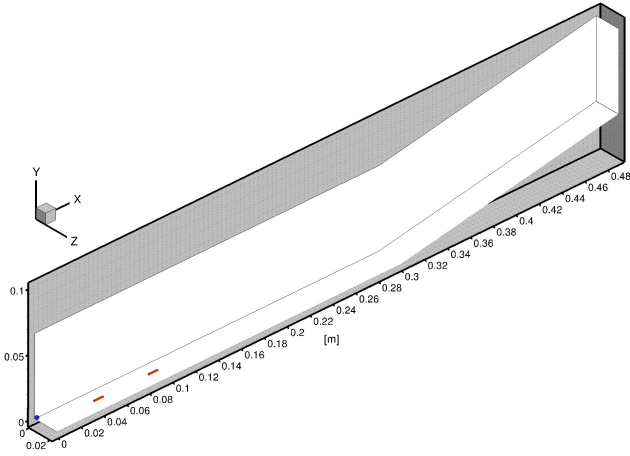
Table 2. Geometric parameters

Parameter	Value	Parameter	Value
L_x	0.400 [m]	I_x	8 [mm]
L_z	0.021 [m]	I_z	2 [mm]
L_y	0.065 [m]	E_x	6
L_c	0.300 [m]	E_z	1
θ	10 [°]	k	1 [mm]

Fig. 1. Physical domain, the orange boxes indicate the positions of the patches.

The peak height of the roughness elements is $k = 1mm$. For the conditions considered in the present study, this yields a value of the k/δ ratio (δ being the boundary-layer thickness) of 0.621 and 0.439 at $RP1$ and $RP2$, respectively. The corresponding critical Reynolds numbers, defined as $Re_{kk} = \rho_k u_k k/\mu_k$ (the subscript k denoting flow properties at the roughness height k), are about 370 and 150, respectively. Table 2 sums up the geometric parameters of the domain, while figure 2 shows a close-up of one of the roughness patches.
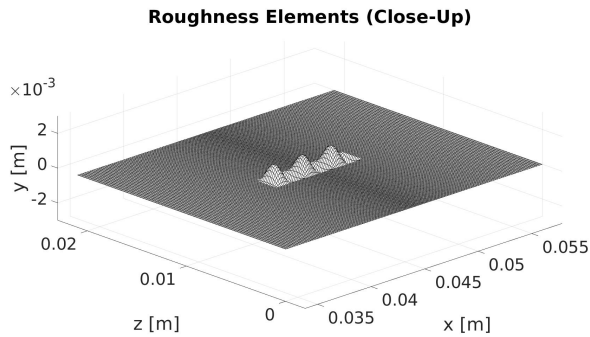

Fig. 2. Detailed view of the roughness patch ($RP1$).

2.2. Governing Equations

Direct Numerical Simulations are performed. Hence, the full three-dimensional Navier–Stokes equations are solved. The temperatures reached within the domain are too low to trigger any considerable chemical reaction. Thus, the ideal gas law is used to close the set of the equations. Therefore, the standard-air specific-heat coefficients for constant pressure (c_P) and volume (c_V) are employed, giving a constant value of $\gamma = 1.4$. The temperature-dependent dynamic viscosity (μ) is computed using Sutherland's law with $S_1 = 110.3K$, while the thermal conductivity is calculated as $\lambda_T = \mu c_P/Pr$, using a constant Prandtl number $Pr = 0.72$.

2.3. Numerical Setup and Procedure

The semi-commercial solver Navier-Stokes Multi Block (NSMB), a finite-volume based code, is used to perform the Direct Numerical Simulations. The code has been employed in hypersonic flow calculations for many years now [26, 27, 28, 11, 17] and allows for parallel computations on structured grids with multiple blocks using the MPI protocol. In the present study, a fourth-order central scheme is used for the spatial discretization. The steady state solution is achieved through a pseudo-time integration with an implicit Euler scheme based on a lower-upper symmetric Gauss-Seidel method. For the unsteady calculations, an explicit third-order Runge-Kutta scheme is used to advance in time, while keeping the choice of the spatial scheme fixed.

Similar grids are employed for both the smooth and the rough cases, with small differences. The same number of points are used in streamwise, wall-normal and spanwise directions ($N_x \cdot N_y \cdot N_z = 4000 \cdot 141 \cdot 256$ nodes). But while the smooth grid has constant-length streamwise elements, in the rough cases the grid cells in the streamwise direction are stretched around the roughness locations. In wall-normal direction, both grids implement a three-layers stretching and hence the wall-normal resolution is the same. The three-layers distribution of the nodes allows to refine the grid in the boundary-layer and separation-bubble regions close to the wall. Finally, in spanwise direction, a constant spacing of the grid lines is employed. The grids are divided in 2400 blocks that can be run in parallel on multiple processors.

Regarding the boundary conditions, six boundaries are

considered. At the inflow, Dirichlet conditions with free-stream flow values are prescribed. At the outflow and upper part of the domain, in order to avoid undesired wave reflections, characteristic variables with extrapolation in space are imposed. In spanwise direction, periodic boundary conditions are given. Finally, at the wall, no-slip boundaries are imposed, together with an adiabatic condition regarding the wall temperature.

For the unsteady simulations, a two-dimensional disturbance field is prescribed at the inflow, on top of the regular steady-state freestream conditions. Similarly to [11], the disturbances are introduced by means of pressure oscillations, defined according to the following formula:

$$p'(y, z, t) = p_0(z) \cdot sin\left(\frac{2\pi y}{\lambda_y}\right) \cdot e^{-(\frac{y}{\delta})^3} \cdot sin(2\pi f t). \quad (2)$$

In this work, $p_0(z) = p_\infty \cdot 10^{-3}$ is constant along the spanwise direction, such that the only spatial variation of the profile is in wall-normal direction. Along the y-direction, the disturbance profile is made of $\lambda_y = 5$ sinusoidal waves, even though it is damped by the exponential function with a value of $\delta = 0.005m$. This ensures that the disturbance is limited to the wall region and interacts only with the boundary layer. Over time, the entire profile oscillates periodically with the frequency $f = 100kHz$.

3. CODE VALIDATION

The code validation was performed against one of the cases shown in [16], namely the $\theta = 18°$ ramp used in the grid convergence study of the reference. This case consists in a Mach 9.1 flow over a fairly high compression corner, which induces the formation of a long separation region with multiple secondary vortices. Table 3 show the freestream conditions used in the validation case. The original simulation was performed on a two-dimensional $4031 \cdot 1009 \simeq 4 \cdot 10^6$ nodes grid, using a second-order upwind method for spatial discretization. The results from NSMB are obtained with a coarser grid ($3500 \cdot 450 \simeq 1.75 \cdot 10^6$ nodes) but a higher-order method (fourth-order central scheme).

Table 3. Flow conditions and wall temperature from [16].

Parameter	Value	Parameter	Value
T_∞	160 [K]	T_w	350 [K]
p_∞	730 [Pa]	ρ_∞	0.016 [Kg/m^3]
U_∞	2280 [m/s]	$Re_{\infty L}$	$3.22 \cdot 10^6$ [m^{-1}]

Overall, a good agreement is obtained. Figures 3 and 4 show the pressure-coefficient (c_p) distribution at the wall and a detail of the recirculation pattern within the separation bubble, respectively. In NSMB (solid line), an almost identical flow separation is obtained, with reattachment just

slightly anticipated. The plateau of the pressure value is consistent with the reference case along the separation region, with a slight discrepancy at reattachment peak. There, NSMB slightly overestimate the pressure coefficient, but the maximum error is within 3%. The development of the secondary vortices inside the bubble is the same, as shown by the streamlines patterns, and so are the compression wave originating from the shear layer at the top of the bubble.
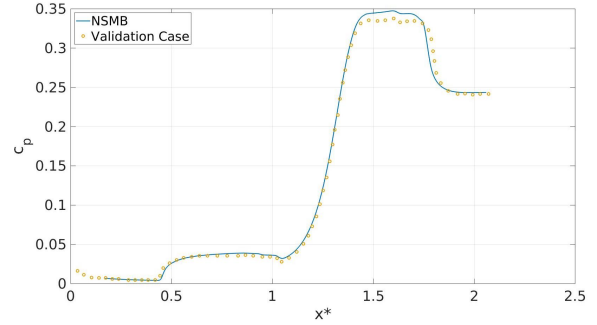

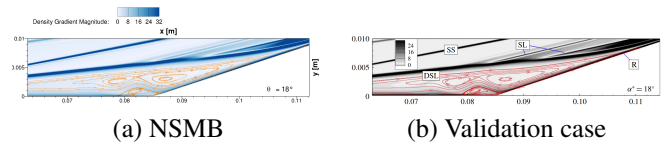**Fig. 3**. Code validation, pressure-coefficient at the wall.

(a) NSMB   (b) Validation case

Fig. 4. Code validation, secondary vortices within the separation bubble.

4. RESULTS

4.1. Smooth reference case

The main results for the smooth case are summarized in figure 5. Looking at the pressure contours, a relatively weak shock can be observed forming right at the leading edge of the flat plate, at the inflow of the domain. Further downstream, a sharper increase in pressure is visible where the boundary layer separates, at $x_{sp} = 0.130m$. In the recirculation region, the pressure is constant, as expected, before undergoing a final and stronger rise once the flow reattaches on the ramp. Regarding the surface temperature, the adiabatic-wall condition allows for a non-uniform temperature distribution. Warmer regions can be noticed downstream of separation and just before reattachment. A marked increase in temperature is, instead, well visible once the flow reattaches on the ramp. Even though the maximum temperatures are in the order of $1600K$, they are not high enough to trigger relevant chemical reactions and, hence, the ideal-gas assumption is acceptable. The black isolines corresponding to a value of streamwise velocity $u = -0.1m/s$ highlight the corrugated pattern

of the reattachment line, in contrast to the straight one at separation point. The mean reattachment position lies around $x_{rt} \simeq 0.435m$. Clearly visible, the flow characterizing the separation bubble is three-dimensional, despite the formally two-dimensional geometry of the problem, indicating a possible global instability of the flow. Along the ramp downstream of reattachment, six streamwise vortices form as shown by the vorticity ω_x slices. These vortices are characterized by relatively low strength, with spanwise velocities of the order of $\pm 10m/s$. Nevertheless, their effect on the wall-temperature distribution is visible, as shown in figure 5, where hot and cold streaks appear on the ramp.
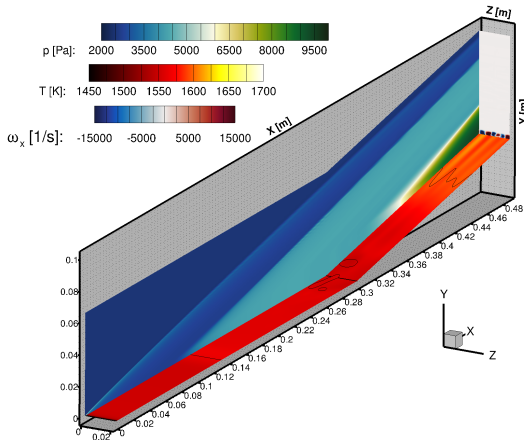
Fig. 5. Smooth case. Pressure contour and wall temperature distribution. Black iso-lines indicate separation and reattachment positions.

4.2. Rough cases: steady conditions

The presence of the roughness patch introduces substantial modifications in the flow field. In the next subsections, the effects of the two patch locations are explained in detail.

4.2.1. RP1

This patch position is the closest to the domain inflow and the farthest upstream with respect to the smooth separation point. As shown in figure 6, the recirculation bubble is smaller than in the reference case. The boundary-layer separation is delayed ($x_{sep} \simeq 0.180m$) and the detached shear layer reattaches earlier on the ramp. The separation line is not straight, but shows a corrugation in the wake of the patch. At reattachment, the roughness induces the formation of a mushroom-shaped structure along the ramp, as shown by the streamwise-velocity contours in figure 7. This structure is a consequence of the streamwise vortices that form in the wake of the roughness elements and are convected by the detached shear layer over the separation bubble. Once the flow reattaches on the

ramp, the vortices are amplified and push slow flow away from the wall. Their effect is also visible on the wall temperature distribution. A high-temperature streak is present downstream of the roughness patch before separation and a stronger one forms at reattachment, just beneath the mushroom structure. The peak temperature is higher than the reference case (up to $\simeq 1700K$), but still not high enough for relevant chemistry effects.
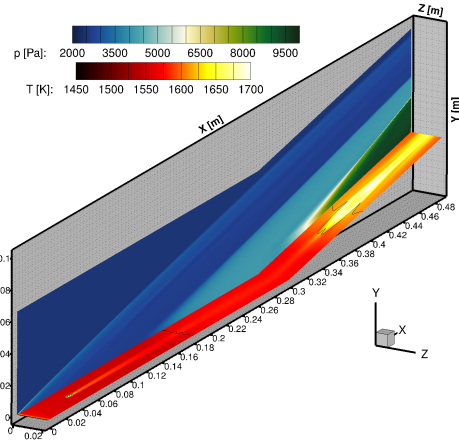

Fig. 6. $RP1$ case. Roughness effects are visible in the temperature distribution and flow separation and reattachment.
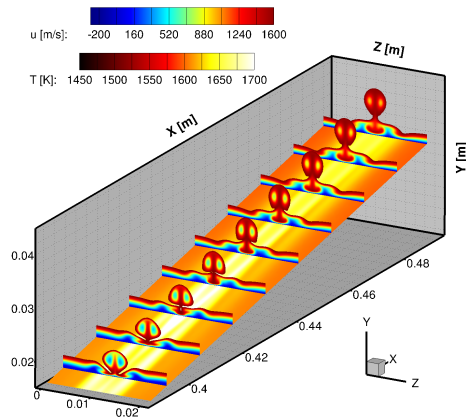

Fig. 7. $RP1$ case. Evolution of the mushroom-shaped structure along the ramp (streamwise-velocity slices cut above $u = 1600m/s$) and wall-temperature distribution.

4.2.2. RP2

With the roughness farther downstream in position $RP2$, a comparable effect is obtained, although some differences stand out with respect to the $RP1$-case. In particular, being the roughness characterized by a smaller Re_{kk}, the position of the boundary-layer separation line is closer to the

smooth case ($x_{sep} \simeq 0.150m$). This results in a longer separation bubble with a delayed reattachment with respect to case $RP1$. Hence, the mushroom-shaped structure forming on the ramp is smaller, as shown in figure 8. Despite this difference, the peak wall-temperature at reattachment reaches around $1700K$ and is comparable to the $RP1$ case. The flow topology in the proximity of the patch is similar in both cases considered here. Figure 9 shows the spanwise velocity distribution around the patch $RP2$ near the wall. The flow opens up as it encounters the roughness elements and then closes again in the wake, forming streamwise vortices. These lose part of their intensity quite quickly. However, what is left of them convects on the separated shear layer and then amplifies once the flow reattaches on the ramp, as visible in figure 10.
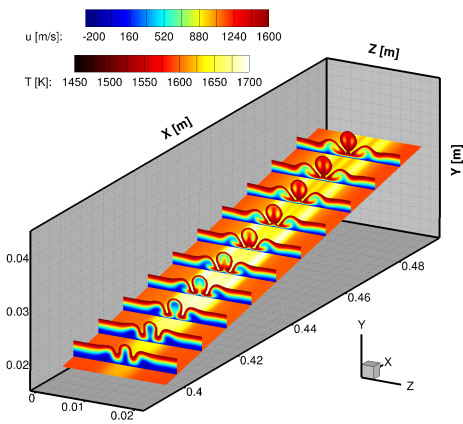

Fig. 10. Spanwise-velocity iso-surfaces ($w = \pm28m/s$) showing the stronger vortices downstream of reattachment.

down within the length of the domain. However, for the $RP2$ case (i.e. the patch characterized by a smaller Re_{kk}), as shown in figures 11 and 12, the flow starts to break down at $x_{br} \simeq 0.445m$. Figure 11 also shows a peak wall-temperature higher ($T_{max} \simeq 1950K$) than the steady case, which is reached as the flow breaks down. In figure 12, the Q-criterion iso-surface coloured with spanwise velocity is displayed. Compared to the steady case (figure 10), it is visible how the features of the vortical structures decrease in size eventually leading to turbulence. A temporal Fourier analysis has been employed to determine the amplitude of the modes present in the flow once disturbances are added. In general, the most amplified mode is the first one, which corresponds to the excitation frequency of $100kHz$. Figure 13 shows the eigenmodes and corresponding amplitudes of the streamwise velocity perturbations (u') at four different stations: downstream of the roughness (a), on the detached shear layer (b,c) and on the ramp (d). The amplitude increases weakly until reattachment and then gets rapidly stronger once the flow reattaches on the ramp, eventually leading to the breakdown of the mushroom structure. As shown in figure 13, the maximum amplitude is reached within the structure forming in the wake of the roughness patch.

Fig. 8. $RP2$ case. Evolution of the mushroom-shaped structure along the ramp (streamwise-velocity slices cut above $u = 1600m/s$) and wall-temperature distribution.
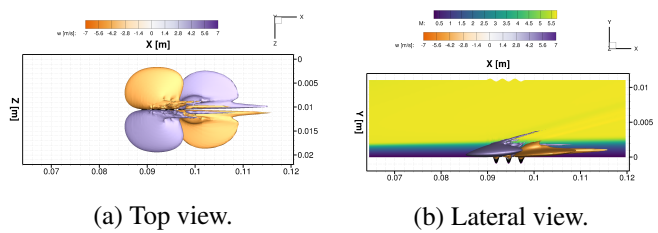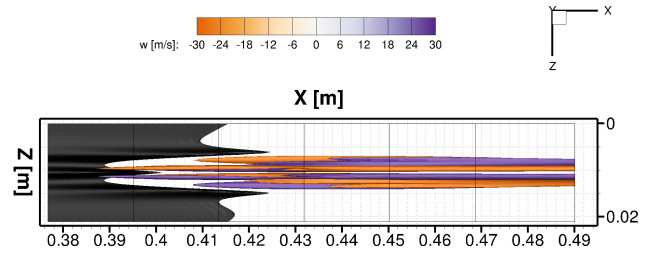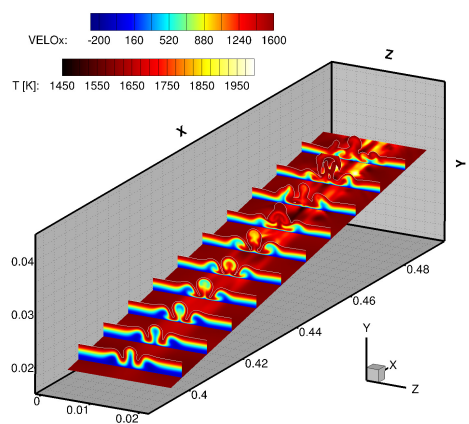

(a) Top view.

(b) Lateral view.

Fig. 9. Spanwise-velocity iso-surfaces ($w = \pm5m/s$). In the lateral view, the centreline slice shows the Mach field.

4.3. Rough cases: unsteady conditions

Starting from the steady state results of the two rough cases, freestream disturbances are introduced at the inflow domain in order to assess their effect on the flow. The major effect can be seen in the reattachment region, once the new boundary layer has formed. In the $RP1$ case, the mushroom structure, although altered, does not entirely break

Fig. 11. $RP2$ unsteady case. Instantaneous streamwise-velocity and wall-temperature distribution.

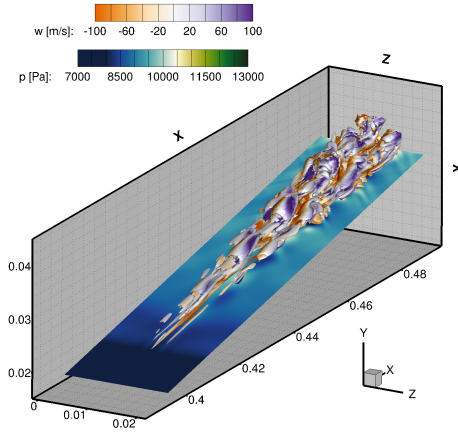**Fig. 12**. *RP*2 unsteady case. Instantaneous Q-criterion iso-surface coloured with spanwise velocity and wall pressure.

(a) At $x = 0.16m$.
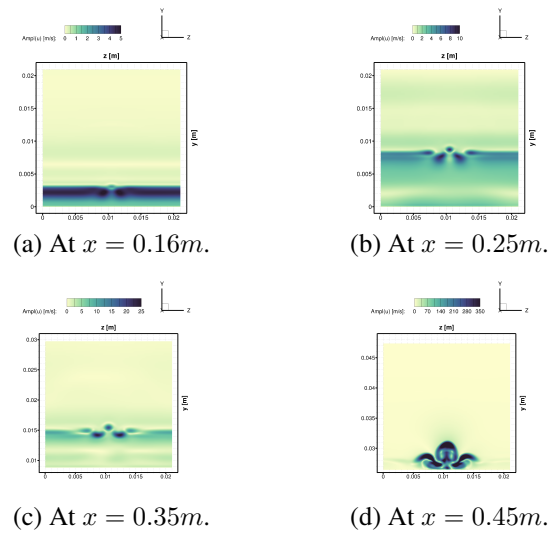
(b) At $x = 0.25m$.

(c) At $x = 0.35m$.

(d) At $x = 0.45m$.

Fig. 13. Case *RP*2. First eigenmodes of streamwise velocity. Note the different colour-scale ranges at the various stations.

5. CONCLUSIONS

DNS have been performed in order to investigate the effects of roughness elements on a Mach 6 ramp flow. A roughness patch made of sinusoidal elements has been placed at two different locations upstream of the corner, before the separation point of the respective smooth configuration. In both cases, the vortices generated by the roughness induce the formation of a mushroom-shaped structure on the ramp, downstream of the reattachment position. This structure dominates the weak streamwise vortices that form on the ramp in the smooth scenario. In the rough cases, remarkably higher wall temperatures can be reached along the ramp as a consequence of the vortices in the roughness wake. The interaction between unsteady freestream disturbances and the roughness flow has also been investigated. The amplitude of the prescribed disturbances is weakly amplified immediately downstream of the roughness and in the separated shear layer. However, once the flow reattaches on the ramp, the magnitude of the perturbed variables rapidly increases, eventually leading to a breakdown of the mushroom structure further downstream of the ramp.

6. ACKNOWLEDGEMENTS

7. REFERENCES

[1] R.M. Cummings, "Critical hypersonic aerthermodynamic phenomena," *Annual Review of Fluid Mechanics*, January 2006.

[2] J.T.C. Liu, "Nonlinear instability of developing streamwise vortices with applications to boundary layer heat transfer intensification through an extended Reynolds analogy," *Philosophical Transactions of the Royal Society*, vol. 366, pp. 2699–2716, May 2008.

[3] P.F. Holloway and J.R. Sterret, "Effect of controlled surface roughness on boundary-layer transition and heat transfer at Mach number of 4.8 and 6.0," *TN D-2054, NASA*, April 1964.

[4] R.M. Hicks and W.R. Harper Jr., "A comparison of spherical and triangular boundary-layer trips on a flat plate at supersonic speeds," *TM X-2146, NASA*, December 1970.

[5] S.P. Schneider, "Effects of roughness on hypersonic boundary-layer transition," *Journal of Spacecraft and Rockets*, vol. 45(2), April 2008.

[6] R.A. King and K.S. Breuer, "Acoustic receptivity and evolution of two-dimensional and oblique disturbances in a Blasius boundary layer," *Journal of Fluid Mechanics*, vol. 432, pp. 69–90, April 2001.

[7] J.P. Van den Eynde and N.D. Sandham, "Numerical simulations of transition due to isolated roughness elements at Mach 6," *AIAA Journal*, vol. 54(1), January 2016.

[8] A. Chou, R.A. King, and M.A. Kegerise, "Transition induced by tandem rectangular roughness elements on a supersonic flat plate," *AIAA Journal*, vol. 54(8), pp. 2322–2337, August 2016.

[9] P. Paredes, M.M Choudari, F. Li, J.S. Jewell, R.L. Kimmel, E.C. Marineau, and G. Grossir, "Nosetip bluntness effects on transition at hypersonic speeds: Experimental and numerical analysis under NATO STO AVT-240," in *AIAA SciTech Forum*, 2018.

[10] S. Hein, A. Theiss, A. Di Giovanni, C. Stemmer, T. Schilden, W. Schröder, P. Paredes, M.M. Choudhari, F. Li, and E. Reshotko, "Numerical investigation of roughness effects on transition on spherical capsules," *Journal of Spacecraft and Rockets*, vol. 56(2), pp. 388–404, March 2019.

[11] A. Di Giovanni and C. Stemmer, "Cross-flow-type breakdown induced by distributed roughness in the boundary layer of a hypersonic capsule configuration," *Journal of Fluid Mechanics*, vol. 856, pp. 470–503, October 2018.

[12] L. Duan, X. Wang, and X. Zhong, "A high-order cut-cell method for numerical simulation of hypersonic-boundary transition with arbitrary surface roughness," in *47th AIAA Aerospace Sciences Meeting Including The New Horizons Forum and Aerospace Exposition*, 2009.

[13] T.V. Poplavskaya and S.V. Kirilovskiy, "Numerical investigation of the influence of the structured surface on disturbance evolution and heat transfer in a hypersonic boundary layer," in *AIP Conference Proceedings 2027, 030019*, 2018.

[14] H. Babinsky and J.K. Harvey, *Shock Wave–Boundary-Layer Interactions*, Cambridge University Press, 2011.

[15] G.L. Korolev, J.S.B. Gajjar, and I. Ruban, "Once again on the supersonic flow separation near a corner," *Journal of Fluid Mechanics*, vol. 463, pp. 173–199, 2002.

[16] S.L. Gai and A. Khraibut, "Hypersonic compression corner flow with large separated regions," *Journal of Fluid Mechanics*, vol. 877, pp. 471–494, August 2019.

[17] G. Chiapparino and C. Stemmer, "Numerical investigation of a Mach 6 hypersonic laminar flow on two-dimensional cold-wall compression corners with controlled surface roughness," *International Journal of Heat and Fluid Flow*, vol. 94, April 2022.

[18] O.R. Burggraf, "Separated laminar boundary layers," *Advances in Engineering Science. NASA Langley Research Center*, vol. 4, 1976.

[19] A. Roghelia, H. Oliver, I. Egorov, and P. Chuvakhov, "Experimental investigation of Görtler vortices in hypersonic ramp flows," *Experiments in Fluids*, vol. 58, 2017.

[20] S. Cao, J. Hao, I. Klioutchnikov, H. Olivier, and C.Y. Wen, "Unsteady effects in a hypersonic compression ramp flow with laminar separation," *Journal of Fluid Mechanics*, vol. 912, 2021.

[21] P. Shrestha, A. Dwivedi, N. Hildebrand, J.W. Nichols, M.R. Jovanovic, and G.V. Candler, "Interaction of an oblique shock with a transitional Mach 5.92 boundary layer," in *46th AIAA Fluid Dynamics Conference*, 2016.

[22] N. Hildebrand, A. Dwivedi, J.W. Nichols, M.R. Jovanovic, and G.V. Candler, "Simulation and stability analysis of oblique shock-wave/boundary-layer interactions at Mach 5.92," *Physical Review Fluids*, vol. 3(1), 2018.

[23] I.V. Egorov, V. Novikov, and A.V. Fedorov, "Direct numerical simulation of supersonic boundary layer stabilization using grooved wavy surface," in *48th AIAA Aerospace Sciences Meeting Including the New Horizon Forum and Aerospace Exposition*, 2010.

[24] M. Choudhari, F. Li, and J. Edwards, "Stability analysis of roughness array wake in a high-speed boundary layer," in *47th AIAA Aerospace Sciences Meeting*, 2009.

[25] A. Wagner, J.M. Schramm, V. Wartemann, G.P. Camillo, H. Ozawa, and J. Steelant, "Boundary layer transition studies on the HEXAFLY-INT hypersonic glide vehicle," in *FAR 2019 - International Conference on Flight Vehicls, Aerothermodynamics and Re-Entry Missions and Engineering*, 2019.

[26] J. Vos, N. Duquesne, and H. Lee, "Shock wave boundary layer interaction studies using the NSMB flow solver," in *3rd European Symposium on Aerothermodynamics for Space Vehicles, ESA SP-426*, 1999.

[27] C. Stemmer, M. Birrer, and N.A. Adams, "Hypersonic boundary-layer flow with an obstacle in thermochemical equilibrium and nonequilibrium," *Journal of Spacecraft and Rockets*, vol. 54(4), pp. 899–915, 2017.

[28] C. Stemmer, M. Birrer, and N.A. Adams, "Disturbance development in an obstacle wake in a reacting hypersonic boundary layer," *Journal of Spacecraft and Rockets*, vol. 54(4), pp. 945–960, 2017.